Faraday Discussions

Cite this: DOI: 10.1039/d3fd00112a



PAPER

View Article Online

Self-sufficient metal—air battery systems enabled by solid-ion conductive interphases†

Shuo Jin,‡^a Shifeng Hong,‡^b Xiaosi Gao,^a Yue Deng,^b Yong Lak Joo[®] and Lynden A. Archer[®]*

Received 29th May 2023, Accepted 4th July 2023

DOI: 10.1039/d3fd00112a

Metal-air batteries including Li-air, Na-air, Al-air, and Zn-air, have received significant scientific and technological interest for at least the last three decades. The interest stems primarily from the fact that the electrochemically active material (O_2) in the cathode can in principle be harvested from the surroundings. In practice, however, parasitic reactions with reactive components other than oxygen in dry air passivate the anode, limit cycling stability of air-sensitive (e.g., Li, Na, Al) and electrolyte-sensitive (e.g., Zn) anodes, in most cases obviating the energy-density benefits of harvesting O2 from ambient air. As a compromise, so-called metal-oxygen batteries in which pure O2 is used as the active cathode material have been extensively studied but are understood to be of little practical relevance because of the large infrastructure required to produce the pure O2 stream. Here, we report on the design of solid-ion conductive chemically inert metal interphases that simultaneously protect a metal anode from parasitic reactions with electrolyte components and which facilitate rapid interfacial ion transport. Interphases composed of indium (In) are reported to be of particular interest for protecting Li and Na anodes from passivation in air whereas interphases composed of Sn are shown to prevent chemical and electrochemical corrosion of Zn anodes in alkaline electrolytes. We report further that these protections enable so-called self-sufficient metal—air batteries capable of extended cycling stability in ambient air environments.

Introduction

Rechargeable metal-air batteries, such as lithium (Li)-air, sodium (Na)-air, and zinc (Zn)-air cells, have attracted considerable research and public attention recently owing to the potentially high energy density they offer.¹⁻⁶ Substantial

^aRobert Frederick Smith School of Chemical and Biomolecular Engineering, Cornell University, Ithaca, NY, 14853, USA. E-mail: laa25@cornell.edu

^bDepartment of Materials Science and Engineering, Cornell University, Ithaca, NY, 14853, USA

[†] Electronic supplementary information (ESI) available. See DOI: https://doi.org/10.1039/d3fd00112a

[‡] These authors contributed equally to this work.

progress has been made in recent years to comprehend the working mechanisms at the electrode level, as well as in the design of electrolytes that enhance the electrochemical cycling stability at the anode and cathode. Nevertheless, uncontrolled and typically parasitic reactions with components other than oxygen in air have resulted in an almost universal focus on related metal–oxygen batteries, in which storage of pure O₂ gas (>99%) (Fig. 1a and b) as part of the battery system adds weight, complexity, and eliminates most (typically all) of the purported advantages of metal–air batteries. The gas storage chambers needed for metal–O₂ batteries are problematic for a variety of additional reasons. They add significantly to the cost of energy storage (O₂ must be purified, compressed, and contained in a leak-proof vessel). Additionally, special safety equipment must be colocated with the battery systems to respond to inadvertent O₂ leaks, fires, or explosions. Additionally energial metal–air batteries, which harness O₂/CO₂ directly from ambient air, are understood to be required for the theoretical benefits of metal–air battery systems to be realized in practice (Fig. 1c and d).

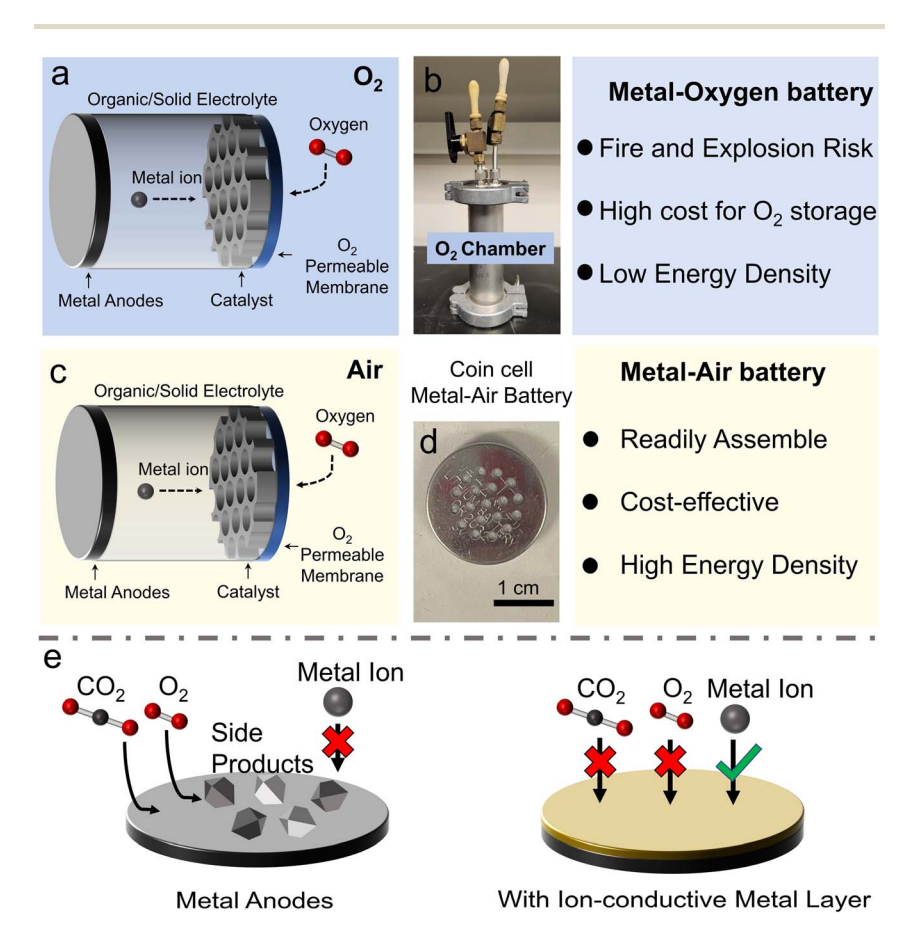


Fig. 1 Metal—oxygen and metal—air batteries. Schematic illustration and picture of metal—oxygen (a) and (b) and metal—air (c) and (d) battery cell configurations used in the study. (e) Schematic illustrating the hypothesized mechanism by which the solid-ion conductive metal alloy layer protects the metal anode from passivation.

In designing such self-sufficient, rechargeable metal-air battery systems, the reversibility of electrochemical transformations at both the cathode and anode in an ambient air environment are important. It is already known through experiments and theoretical analysis1-5 that accumulation of highly nucleophilic and electrically insulating Li₂O₂ particles in the cathode limits discharge capacity of Li-O₂ batteries. These limits can be overcome to a degree in high Gutmann donornumber electrolyte solvent environments, which simultaneously lower the Li₂O₂ nucleation rate in the cathode and are stable against nucleophilic attack by Li₂O₂. The stability of the metal anode in an air environment poses an even more critical concern, particularly for batteries based on air-sensitive anodes such as Li and Na. 19,20 It is generally believed that Li and Na are unstable in the atmospheric environment due to the chemical reaction between the metal and oxygen, moisture (H₂O), or both.^{21,22} Interestingly, even after removing moisture from an air source by means of a super-hydrophobic membrane (such as PTFE) (Fig. 1c and d), Li/Na-air batteries have been reported to exhibit limited cycle life, and to fail by an "over-potential run-away" mechanism indicative of electrolyte degradation or electrode passivation. Furthermore, even Zn, which is an air-stable anode, is compromised by chemical and electrochemical instability in typical alkaline electrolytes used in Zn-air batteries (e.g., 6 M KOH + 0.2 M ZnO), resulting in poor long-term cycling performance of such cells. 9,23,24

To address these challenges, the failure mechanisms of Li metal anodes in rechargeable Li–air batteries cycled in an ambient air environment were investigated. Surprisingly, we discovered that the dominant failure mode of the anode is triggered not by parasitic reaction with other Li-reactive gases (e.g., CO_2 or N_2) present in ambient air, but from formation of large amounts of lithium peroxide (Li_2O_2) on the anode. It was discovered further that these effects are exacerbated under cell-running conditions in which the O_2 concentration is lower. These findings contrast with analogous experimental observations for Na–air cells, wherein CO_2 in ambient air is found to be the primary component responsible for chemical degradation and passivation of the battery anode.

We hypothesized that thin, gas impermeable, and chemically inert interphases formed directly on Li/Na would limit chemical reaction with dissolved species in the electrolyte. A further hypothesis is that if the interphases are composed of metals capable of alloying with Li/Na and of facilitating fast ion/atom transport from the metal–electrolyte interface (Fig. 1e), it should be possible to fully isolate electrochemical transformations at the metal from atmospheric species dissolved in the electrolyte. Of particular note is that a 35 μ m thick indium (In) interphase meets all of the above requirements and when deployed in metal–air battery cells, provides exceptional protection for both Li and Na metal anodes. In contrast, for Zn anodes in aqueous alkaline electrolytes, an interphase composed of tin (Sn) was observed to provide sufficiently fast ion transport and to simultaneously suppress the chemical and electrochemical reactions between the Zn anode and alkaline electrolytes.

Experimental procedures

Materials

In(OTf)₃, Sn(OTf)₂, DME, LiTFSI, LiNO₃, NaClO₃, diglyme, KOH, ZnO, and SuperP carbon were purchased from Sigma Aldrich. For the Li–air battery systems used in

the study, dimethyl ether (DME) was used as the electrolyte solvent and a 2 M LiTFSI + 0.5 M LiNO₃ cocktail used as the electrolyte salt. For the Na-air battery systems, the electrolyte solvent is diglyme and 1 M NaClO₃ used as the salt. Finally, the Zn-air battery systems used in the study employed an aqueous electrolyte containing 6 M KOH and 0.2 M ZnO. To create Li@In and Na@In anodes for our study, pure Li and Na foil were soaked in a 0.5 M In(OTf)₃-DME electrolyte for 10 min. An analogous procedure was used to create Zn@Sn anodes, except a 0.5 M Sn(OTf)₂ aqueous electrolyte was used to pretreat the Zn foil electrode. Additionally, during cycling of the Li@In and Na@In anodes, 20 mM In(OTf)₃ was added to the DME and diglyme electrolytes.

Electrochemical measurements

Galvanostatic charge/discharge characteristics of electrodes and electrolytes were studied in CR2032 coin cells. A Neware battery test system operated at room temperature (25 °C \pm 1 °C) and without use of a climatic/environmental chamber was employed for our experiments. The area of electrodes in this study were maintained fixed at 0.3175 cm². The Li–air batteries were assembled using a 0.75 mm thick Li foil as anode. A 9:1 mixture of SuperP carbon and a PVDF binder were coated on a 3D carbon paper at a mass loading of 3 mg cm $^{-2}$ and used to fabricate the porous, air cathode. An Al $_2$ O $_3$ coated Celgard membrane was employed as separator. Approximately 20 μ L electrolyte was added to each coin cell. An analogous battery configuration was used for the Na–air cells, except the Li foil was replaced with Na of approximately the same thickness. In contrast, for the Zn–air batteries, the air cathode was formed using a Pt/C and Ir/C material purchased from the Fuel Cell Store. The material was first dispersed in an ethanol solution (1:1) with 3 wt% Nafion and, finally, coated on carbon paper at a mass of 3 mg cm $^{-2}$ to create the porous cathodes.

Materials characterization

Interfacial transport properties were investigated using electrochemical impedance spectroscopy (EIS) measurements using a BioLogic Potentiostat. Powder X-ray diffraction analysis was performed on a Bruker D8 Advance ECO powder diffractometer with a Cu K α X-ray source used to characterize the crystal structure of the metal@metal anodes. Field-emission scanning electron microscopy (FESEM) was carried out on a Zeiss Gemini 500 Scanning Electron Microscope to study the electrodeposition morphology of Li electrodeposits. XPS were analyzed using a Surface Science Instruments SSX-100 ESCA Spectrometer with operating pressure $\it ca.~1~\times10^{-9}$ Torr. Monochromatic Al K α X rays (1486.6 eV) with photoelectrons collected from a 800 μm diameter analysis spot. Photoelectrons were collected at a 55° emission angle with source to analyzer angle of 70°. A hemispherical analyzer determined electron kinetic energy, using a pass energy of 150 eV for wide/survey scans, and 50 eV for high resolution scans. A flood gun was used for charge neutralization of non-conductive samples.

DFT analysis of migration energy barriers

Migration energy barriers for Li⁺ in various metal electrodes were calculated using first-principle calculations conducted within the framework of density functional theory (DFT), as implemented in the Quantum ESPRESSO package (ver6.4.1).

Pseudopotentials were obtained from the standard solid-state pseudopotentials (SSSP) library, generated from the Perdew–Burke–Ernzerhof (PBE) exchange-correlation functional along with generalized gradient approximation (GGA). Energy cutoffs were set to 30 and 240 Ry for the plane-wave basis and electron density representation. Electron convergence threshold was set to 10^{-7} Ry. Gaussian smearing was incorporated into the electron occupations. We considered a $2 \times 2 \times 2$ supercell of body-centered tetragonal indium metal (space group I4/mmm, a = 3.2523 Å, c = 4.9461 Å), sampled with $6 \times 6 \times 6$ Monkhorst–Pack k-point mesh.

The minimum energy paths (MEPs) for ${\rm Li}^+$ jumps in an indium metal lattice were calculated from the climbing-image nudged elastic band (CI-NEB) method. In a typical MEP, one indium atom was replaced by lithium, which migrates to an immediately adjacent vacancy that is meanwhile symmetrically equivalent. Before MEP calculations, all initial structures and end structures were allowed to fully relax with a force convergence threshold of 10^{-3} a.u. Each MEP was divided into 7 "images" (atomic positions), where energies and energy gradients were evaluated to interpolate the MEP energy profile. Convergence threshold of the total force on each image was set to 0.05 eV Å⁻¹. Finally, the crystal structures were visualized with the help of XCrysDen and BURAI.

Physical and electrochemical characteristics of pure Li anode in Li-air batteries

To study self-sufficient Li-air batteries, battery cells in which pristine Li metal served as anode and SuperP conductive carbon as the current collector for the porous air cathode were constructed. On the air-exposure side, three layers of a breathable waterproof membrane (hydrophobic PTFE) was used to isolate the cell from moisture in the air and dimethoxyethane (DME) + 2 M LiTFSI + 0.5 M LiNO₃ was employed as electrolyte. As shown in Fig. 2a, the Li-air cells fail quickly (after approximately three cycles) in an open-air environment. The results show that the discharge voltage decreases from 2.3 V (vs. Li/Li⁺) in the first two cycles to a negative value of -3 V (in the 8th cycle), indicating complete failure of the batteries. After eight cycles, the Li anode was harvested and imaged (see Fig. 2b). Compared to the clean and shiny surface of pristine Li foil before cycling, the Li anode harvested from the failed cells all possess a thick white powder-like overcoat, that completely covers the Li anode. X-ray diffraction (XRD) analysis revealed that the layer is composed of the non-ion conductive Li₂O₂ material (Fig. 2c). Furthermore, the XRD patterns obtained from 24-hour aged Li anode, and Li anodes harvested at the 4th and 8th cycles clearly show that Li₂O₂ is formed under all these conditions. Fig. 2f, g and S1[†] report results from SEM analysis of the electrodes. The results indicate that the Li anode collected after eight cycles is covered with a coarse non-conductive material with a thickness of approximately 65 μm. The XRD analysis indicates that this material is Li₂O₂. In contrast, SEM analysis shows that the surface of the pristine Li foil before cycling is smooth and clean (Fig. 2d and e). X-ray photoelectron spectroscopy (XPS) analysis confirmed the presence of Li₂O₂ interphase on the Li anode surface, with a high oxygen ratio of about 38% (Fig. 2h), *i.e.*, close to the Li content (\sim 50%) and significantly higher than the fluorine ratio (\sim 7%). High-resolution analysis further validated the

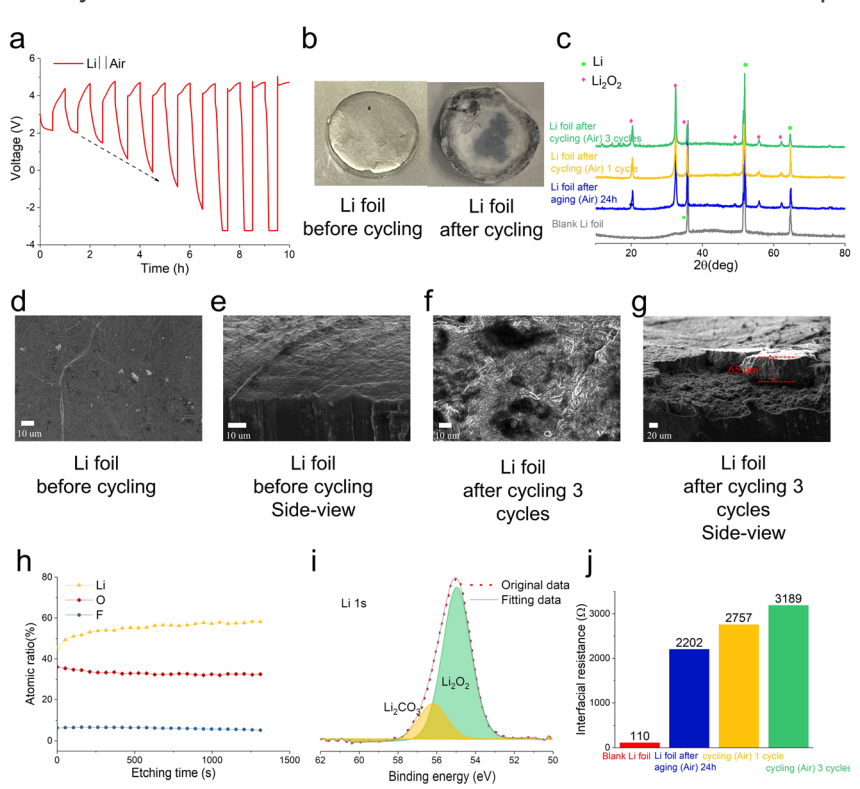


Fig. 2 Electrochemical and material properties of lithium metal anode used in rechargeable Li||air batteries. (a) Galvanostatic discharge and charge profiles for Li||air cells. (b) Optical images of lithium foil before and after cycling. (c) X-ray diffraction pattern obtained using pristine lithium foil, aged lithium foil, and cycled lithium foil. Scanning electron microscope images obtained using (d) lithium foil before cycling, (e) side-view of lithium foil before cycling, (f) lithium foil after 3 cycles, and (g) side-view of lithium foil after 3 cycles. (h) Atomic concentration profile of Li, O and F *versus* etching time determined from XPS analysis. (i) Li 1s XPS spectra of cycled lithium foil. (j) Interfacial resistance of pristine lithium foil, aged lithium foil, and cycled lithium foil deduced from EIS analysis.

presence of $\mathrm{Li_2O_2}$ (Fig. 2i and S2†). Therefore, it can be concluded that the $\mathrm{Li_2O_2}$ interphase plays a key role in the electrochemical characteristics of the Li anode in Li–air cells; its large thickness and poor conductivity also readily explains the rapid failure of the Li–air batteries.

To further assess this conclusion, the Li metal anode surface was studied after cycling in cells where ambient air or pure $\rm O_2$ was used as the active material in the cathode. Interestingly, unlike the $\rm Li_2O_2$ passivating layer found in the Li–air cells, a LiOH coating is observed on the Li metal surface after cycling in a pure $\rm O_2$ environment (Fig. S3a†). Electrochemical impedance spectroscopy (EIS) analysis indicates that the $\rm Li_2O_2$ coating has a high interfacial resistance, which increases from approximately 110 ohm to over 2000 ohm after aging or cycling (Fig. 2j). This increased interfacial resistance explains the rapid discharge voltage decrease of Li–air batteries shown in Fig. 2a. In contrast, the stable and low interfacial resistance of the LiOH coating formed in the $\rm O_2$ environment (Fig. S3b†) is

evidently a key to the long-term cycling stability of Li- O_2 battery cells. It was conjectured that the different passivating films (Li₂ O_2 νs . LiOH) arises from differences in the composition of atmospheric gases dissolved in the electrolyte. Specifically, in a dilute oxygen environment such as air, Li metal, and O_2 are unable to fully react, resulting in the formation of Li₂ O_2 , with low ion conductivity and high nucleophilicity. Conversely, in a pure oxygen environment, O_2 can activate the organic electrolyte and, even in the absence of moisture, promote the decomposition of the electrolyte to form LiOH. These disparate reaction products at the metal-air and metal- O_2 battery anode result in very different cycling abilities. We therefore hypothesized that protecting the Li anode with an inert metal coating capable of providing fast ion transport would prevent anode passivation by Li₂ O_2 , extending the cycle life of Li-air cells.

Selecting In as an interphase for Li/Na

To choose the most suitable protective interphase for the Li metal anode, the migration energy barriers of the following materials capable of forming alloys with Li were determined: silicon (Si), aluminum (Al), tin (Sn), indium (In), *etc.* (Fig. 3a) were firstly compared.²⁵⁻²⁸ Among the various alloy materials, it was found that In

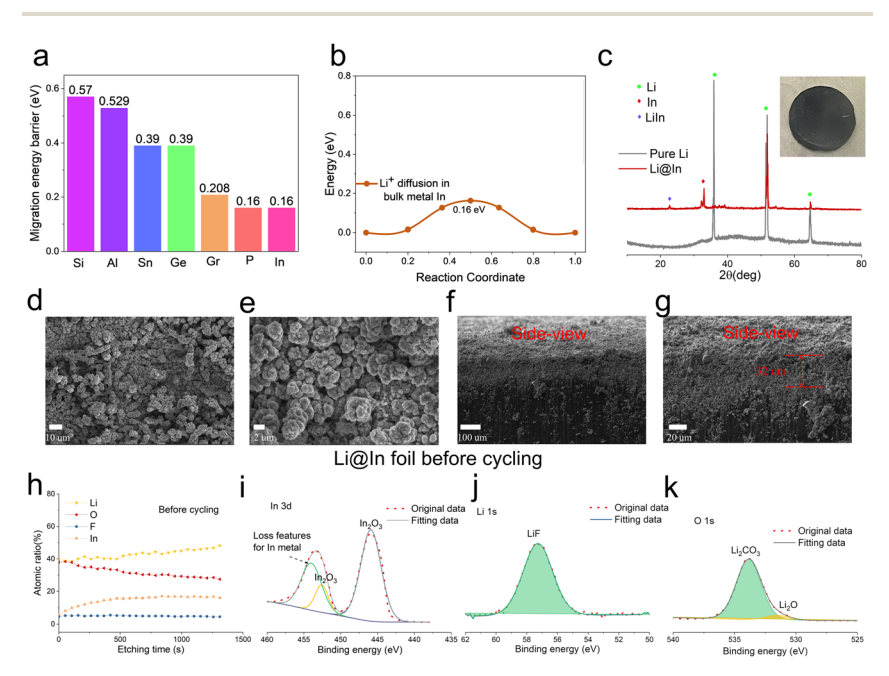


Fig. 3 Material characterization of lithium foil protected by an In metal interphase. (a) Calculated migration energy barrier for lithium ion in various anode candidate materials. (b) Detailed lithium-ion diffusion energy *versus* reaction coordinate in In. (c) XRD analysis of pristine Li and Li@In anodes. Inset: optical image of Li foil with solid-ion conductive metallic interphase. (d) and (e) Top-view SEM micrographs of Li@In foil at different size scales. (f) and (g) Side-view SEM images of Li@In at different magnifications. (h) Atomic concentration profile of Li, O, F and In *versus* etching time evaluated using XPS. (i) In 3d XPS spectra of pristine Li@In foil. (k) O 1s XPS spectra of pristine Li@In foil.

shows the lowest Li^+ migration energy barrier (~ 0.16 eV) (Fig. 3b and S4†), indicating that the Li⁺ is capable of transporting through an In interphase with low overpotential. To assess this assumption, a facile ion exchange procedure reported before²⁹⁻³¹ was used to construct the In interphase on the Li metal surface. Here, the pristine Li foil was soaked in the DME + 0.5 M In(OTf)₃ electrolytes for 10 min to obtain the Li@In anode. As shown in Fig. 3c-g and S5,† the Li metal surface was covered by dense In layers with a thickness of approximately 32 µm. The In layer was confirmed by the XRD and XPS results. In Fig. 3c, the LiIn alloy and In signal peaks were observed after ion exchange reaction between Li metal and In3+. Importantly, in contrast to previous works where only alloy interphase forms, 30,31 In metal signal was found on the Li@In metal surface due to a high concentration of In³⁺ in 0.5 M In(OTf)₃ solution. Moreover, as shown in Fig. 3h and i, the existence of In metal was further confirmed by XPS results, in which a peak located at 454 eV indicates the loss feature of In metal. On the other hand, the observed In₂O₃ signal peaks should result from the inevitable contact between the In metal and air. Furthermore, sputtering experiments revealed the ratio of different elements on the top layer of the In metal interphase, in which the In ratio increases from 5% on the surface to 18% as sputtering thickness increases (Fig. 3h). LiF, LiCO₃ and Li₂O signals (Fig. 3j and k) were also observed which may come from the chemical reaction between Li metal and anion (OTf)-.30

Significantly, the cycling performance of the Li-air batteries in an ambient air environment was improved by more than thirty fold (from 4 h to over 140 h at 1 mA cm⁻², 1 mA h cm⁻²) (see Fig. 4a). These findings confirm that the combination of the surface protective effect of the In interphase and facile Li⁺ transport through the layer are effective in limiting Li metal anode passivation in an air environment. Moreover, as Fig. 4b shows, the voltage gap between discharge $(\sim 2.6 \text{ V})$ and charge process $(\sim 3.3 \text{ V})$ is about 0.7 V, indicating that transport of Li⁺ across the In interphase adds negligibly to the overpotential. XRD analysis reported in Fig. 4c show further that the In protective interphase is stable. The In XRD peaks are in fact clearly observed for Li@In anodes harvested after aging for 24 hours, cycling for 10 times and 20 times respectively. The morphology of the anodes deduced from SEM top-view and side-view images of the In layer provide additional confirmation of the stability of the In interphase. As shown in Fig. 4g-j, the In layer maintained its compact form after 20 cycles in the Li-air cells. We note, however, that results from EIS analysis indicate that after aging for 24 hours, the interfacial resistance of the Li@In anode increased from 556 ohm to 864 ohm (Fig. 4d). Moreover, during the cycling process, the interfacial resistance is observed to increase from 556 ohm to about 1000 ohm, and this value was maintained stable in different cycles (5th-80th) (Fig. 4e and f).

XPS analysis provides a partial explanation of the resistance increase. Sputtering experiments show that after cycling, the In content decreased from 18% (Fig. 3h) to 10% (Fig. 4k), while the fluorine content increased from 5% to 22%. It means that while on the one hand more inorganic LiF is formed on the electrode during cycling (Fig. 4i); on the other hand, the top layer of the protective In coating is oxidized to form In₂O₃. This is confirmed by the results reported in Fig. 4m, where compared to the In signal before cycling (Fig. 3i), the ratio of the In metal to In₂O₃ decreased. Furthermore, only a minor Li₂O signal was observed (Fig. 4n). Based on these results, we conclude that a fraction of the In metal on the top was oxidized to In₂O₃, protecting the Li metal electrode, but increasing the

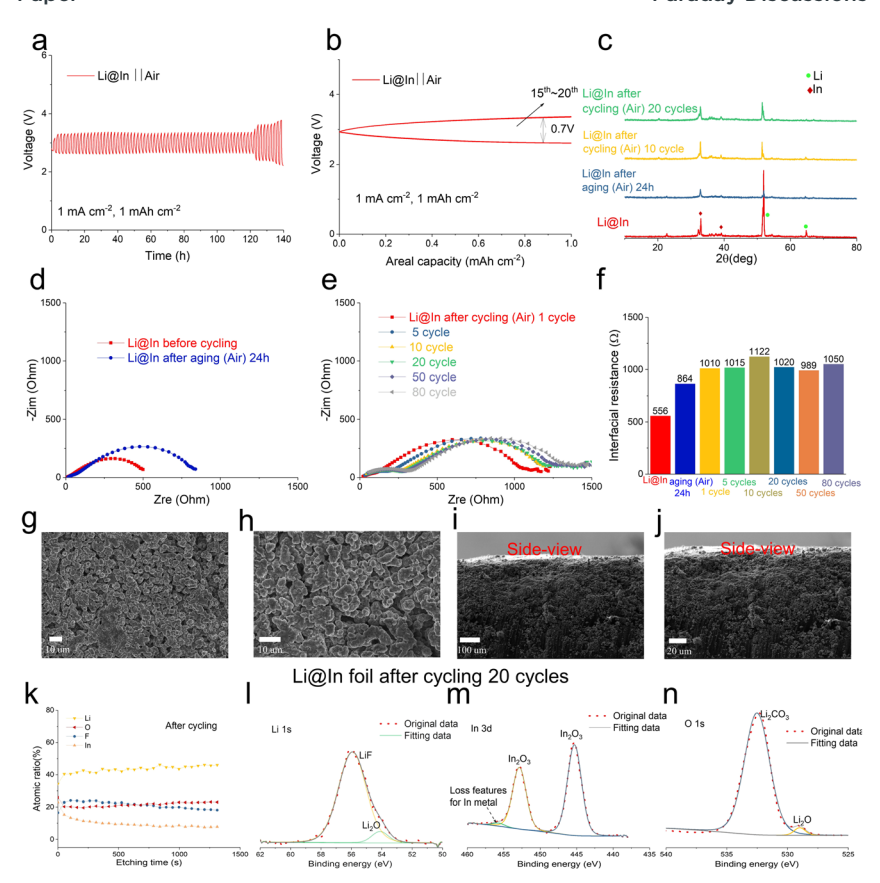


Fig. 4 Electrochemical performance of Li@In||air cells and postmodern characterization of the electrodes. (a) Galvanostatic discharge and charge profiles of Li@In||air cells with respect to time. (b) Galvanostatic discharge and charge profiles of Li@In||air cells with respect to capacity. (c) XRD pattern of pristine Li@In anode, aged Li@In anode and cycled Li@In anode. (d) EIS analysis result of pristine Li@In||air cell and aged Li@In||air cell. (e) EIS analysis result of Li@In||air cell at different cycle number. (f) Interfacial resistance of pristine Li@In||air cell, aged Li@In||air cell and cycled Li@In||air cell. (g) and (h) Top-view SEM images of cycled Li@In foil. (ii) and (j) Side-view SEM images of cycled Li@In foil. (k) Atomic concentration profile of Li, O, F and In collected from cycled Li@In foil. (l) Li 1s XPS spectra of cycled Li@In foil. (m) In 3d XPS spectra of cycled Li@In foil. (n) O 1s XPS spectra of cycled Li@In foil.

interfacial resistance. On the basis of the findings thus far, we conclude further that the extended cycling life of Li@In-air cells achieved is attributable to the combined protective effect and low transport barrier to Li⁺ diffusion produced by the In solid-ion conductive interphase.

Extension to other rechargeable metal—air batteries: Na—air and Zn—air

The stability of the In solid-ion conductive interphase suggests that a metal@-metal anode design concept might be applicable as a universal procedure for

stabilizing the metal anode in rechargeable metal-air batteries suitable for cycling in an ambient air environment. Hence, the efficacy of the protective layers in Na-air and Zn-air batteries was evaluated. Given the similarity between Li and Na, the In interphase was employed for Na metal. Similar to the strategy employed to create a stable interphase for the Li metal anode, the failure mechanism of the Na anode in Na-air cells during extended cycling was firstly explored. Unlike the Li anode, the Na-air battery could cycle 90 times without any protective layers on the Na anode (Fig. 5a), suggesting that the failure mechanism between Li and Na might differ. 32 XRD results (Fig. S6†) revealed that, unlike the Li anode, the Na anode is significantly more reactive to CO2, resulting in the formation of Na2CO3 on the Na anode surface after cycling. Compared to the smooth morphology of the Na anode surface, the formation of Na₂CO₃ results in a rugged appearance, as displayed in Fig. S7.† Therefore, the same In protective layer was applied on the Na anode surface. After similar ion-exchange reactions, the Na surface was covered with dense In layers (Fig. 5b-d), which was further validated by the In signal peaks in the XRD results (Fig. 5b). Significantly, the cycling stability of Na@In-air batteries increased from 90 h to over 140 h (Fig. 5a). XRD results and the morphology of the Na anode (Fig. 5b-d and S8†) demonstrated the stability of the In protective layers after cycling.

Finally, the interphase design concept was extended to Zn-air battery systems. The issues with the Zn anode in the alkaline electrolytes have been extensively

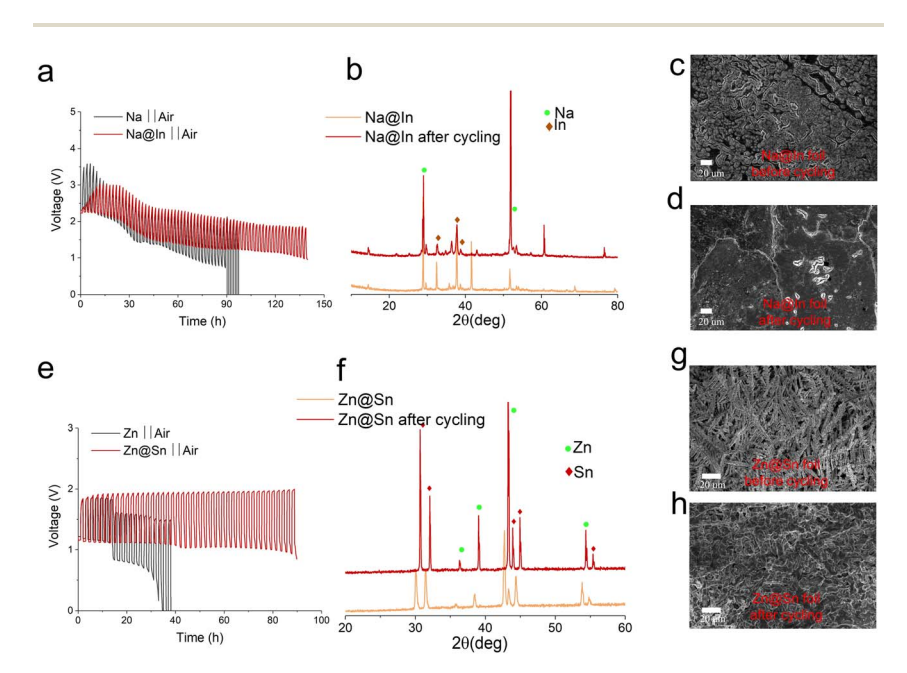


Fig. 5 Material characterization of Na@In anode and Zn@Sn anode and their electrochemical performance in Na@In $\|$ air and Zn@Sn $\|$ air battery. (a) Galvanostatic discharge and charge profiles of Na $\|$ air and Na@In $\|$ air cells. 1 mA cm $^{-2}$, 1 mA h cm $^{-2}$. (b) XRD pattern of pristine Na@In anode and cycled Na@In anode. SEM images of Na@In anode (c) before cycling and (d) after cycling. (e) Galvanostatic discharge and charge profiles of Zn $\|$ air and Zn@Sn $\|$ air cells. 1 mA cm $^{-2}$, 1 mA h cm $^{-2}$. (f) XRD pattern of pristine Zn@Sn anode and cycled Zn@Sn anode. SEM images of Zn@Sn anode (g) before cycling and (h) after cycling.

discussed in previous reports. In brief, the non-conductive ZnO layer due to the chemical and electrochemical side reactions between the Zn anode and the alkaline electrolyte is the primary cause of rapid failure in Zn-air batteries. The experimental findings confirm this observation (Fig. 5e, S6 and S9†). Analogous to what is observed for Li and Na, a solid metal interphase is an appropriate choice for the Zn anode as it can suppress the chemical and electrochemical side reactions and serve as a solid ion conductor. According to these requirements, tin (Sn) is considered to be an interphase material. After the facile ion exchange reaction between Zn anode and Sn²⁺, dendritic Sn metal covers the entire surface of the Zn. The existence of Sn metals is confirmed by XRD (Fig. 5f–h). With the protection of the Sn layer, the cycling performance of Zn@Sn–air batteries is improved from approximately 30 h to over 90 h (Fig. 5e). The XRD and morphology of the Zn@Sn anode (Fig. 5f–h and S10†) after cycling indicate the stability of the Sn protective interphase.

In conclusion, failure modes of various metal anodes in electrochemical cells in which molecular species contained in ambient air serve as the active material in the cathode were studied. Such cells are of particular interest because they preserve the intrinsic advantages of metal–air battery systems, without the need for expensive gas purification and ancillary equipment for storing and dispensing oxygen as required for metal–O₂ batteries. It has been shown that a general strategy, in which a chemically inert metal (e.g., In or Sn) capable of facilitating rapid Li/Na/Zn ion/atom transport away from the electrolyte–anode interface is used as a protective interphase for the anode, provides an effective strategy for extending anode lifetime in any metal–air battery. The approach has been demonstrated to extend the cycling life of Li/Na/Zn–air batteries. It is envisioned that refinement of this strategy to facilitate use of the metal@metal anodes in tandem with high DN electrolytes will provide fresh approaches for creating self-sufficient Li–air and other metal–air batteries that exhibit performance features that live up to the potential suggested by their chemistry.

Data availability

All data needed to evaluate the conclusions in the paper are present in the paper or the ESI.†

Author contributions

S. J. and L. A. designed the experiments. All authors assisted in data analysis and writing and editing of the manuscript.

Conflicts of interest

The authors declare that they have no competing interests.

Acknowledgements

This work was supported as part of the Center for Mesoscale Transport Properties, an Energy Frontier Research Center supported by the U.S. Department of Energy, Office of Science, Basic Energy Sciences, under award #DE-SC0012673. This work

made use of the Cornell Center for Materials Research Shared Facilities which are supported through the NSF MRSEC program (DMR-1719875).

References

- 1 D. Aurbach, B. D. McCloskey, L. F. Nazar and P. G. Bruce, Advances in understanding mechanisms underpinning lithium-air batteries, *Nat. Energy*, 2016, 1, 16128.
- 2 S. K. Das, S. Lau and L. A. Archer, Sodium-oxygen batteries: a new class of metal-air batteries, *J. Mater. Chem. A*, 2014, **2**, 12623–12629.
- 3 S. K. Das, *et al.*, High energy lithium–oxygen batteries transport barriers and thermodynamics, *Energy Environ. Sci.*, 2012, 5, 8927–8931.
- 4 N. Imanishi, A. C. Luntz and P. G. Bruce, *The lithium air battery: fundamentals*, Springer, 2014.
- 5 S. Lau and L. A. Archer, Nucleation and Growth of Lithium Peroxide in the Li-O₂ Battery, *Nano Lett.*, 2015, **15**, 5995–6002.
- 6 J.-N. Liu, et al., A brief history of zinc-air batteries: 140 years of epic adventures, Energy Environ. Sci., 2022, 15, 4542-4553.
- 7 Y. Chen, S. A. Freunberger, Z. Peng, O. Fontaine and P. G. Bruce, Charging a Li-O₂ battery using a redox mediator, *Nat. Chem.*, 2013, 5, 489–494.
- 8 S. Choudhury, *et al.*, Designer interphases for the lithium-oxygen electrochemical cell, *Sci. Adv.*, 2017, 3, e1602809.
- 9 S. Jin, *et al.*, Zwitterionic Polymer Gradient Interphases for Reversible Zinc Electrochemistry in Aqueous Alkaline Electrolytes, *J. Am. Chem. Soc.*, 2022, **144**, 19344–19352.
- 10 L. Johnson, *et al.*, The role of LiO₂ solubility in O₂ reduction in aprotic solvents and its consequences for Li-O₂ batteries, *Nat. Chem.*, 2014, **6**, 1091–1099.
- 11 J. Lu, et al., A lithium-oxygen battery based on lithium superoxide, *Nature*, 2016, **529**, 377–382.
- 12 Q. Lv, *et al.*, Semiconducting metal-organic polymer nanosheets for a photoinvolved Li-O₂ battery under visible light, *J. Am. Chem. Soc.*, 2021, **143**, 1941–1947.
- 13 S. H. Oh, R. Black, E. Pomerantseva, J.-H. Lee and L. F. Nazar, Synthesis of a metallic mesoporous pyrochlore as a catalyst for lithium-O₂ batteries, *Nat. Chem.*, 2012, 4, 1004–1010.
- 14 Z. Peng, S. A. Freunberger, Y. Chen and P. G. Bruce, A reversible and higherrate Li-O₂ battery, *Science*, 2012, 337, 563–566.
- 15 B. D. Adams, *et al.*, Towards a stable organic electrolyte for the lithium oxygen battery, *Adv. Energy Mater.*, 2015, 5, 1400867.
- 16 M. Asadi, et al., A lithium-oxygen battery with a long cycle life in an air-like atmosphere, Nature, 2018, 555, 502–506.
- 17 F. Wu and Y. Yu, Toward true lithium-air batteries, Joule, 2018, 2, 815-817.
- 18 X. Bi, et al., From sodium-oxygen to sodium-air battery: enabled by sodium peroxide dihydrate, *Nano Lett.*, 2020, **20**, 4681–4686.
- 19 S. Xu, S. Lau and L. A. Archer, CO₂ and ambient air in metal-oxygen batteries: steps towards reality, *Inorg. Chem. Front.*, 2015, 2, 1070–1079.
- 20 T. Zhang and H. Zhou, A reversible long-life lithium-air battery in ambient air, Nat. Commun., 2013, 4, 1817.

- 21 M. Cho, et al., The effects of moisture contamination in the Li-O₂ battery, J. Power Sources, 2014, 268, 565–574.
- 22 B. G. Kim, *et al.*, A moisture-and oxygen-impermeable separator for aprotic Li-O₂ batteries, *Adv. Funct. Mater.*, 2016, **26**, 1747–1756.
- 23 B. E. Hawkins, *et al.*, Electroactive ZnO: Mechanisms, Conductivity, and Advances in Zn Alkaline Battery Cycling, *Adv. Energy Mater.*, 2022, **12**, 2103294.
- 24 D. E. Turney, et al., Rechargeable zinc alkaline anodes for long-cycle energy storage, Chem. Mater., 2017, 29, 4819–4832.
- 25 G. DeLorenzi, C. Flynn and G. Jacucci, Effect of anharmonicity on diffusion jump rates, *Phys. Rev. B: Condens. Matter Mater. Phys.*, 1984, 30, 5430.
- 26 M. S. Kim, et al., Enabling reversible redox reactions in electrochemical cells using protected LiAl intermetallics as lithium metal anodes, Sci. Adv., 2019, 5, eaax5587.
- 27 J. Qu, J. Xiao, T. Wang, D. Legut and Q. Zhang, High rate transfer mechanism of lithium ions in lithium–tin and lithium–indium alloys for lithium batteries, *J. Phys. Chem. C*, 2020, **124**, 24644–24652.
- 28 Z. Wang, *et al.*, Modelling and simulation of electron-rich effect on Li diffusion in group IVA elements (Si, Ge and Sn) for Li ion batteries, *J. Mater. Chem. A*, 2014, **2**, 13976–13982.
- 29 S. Choudhury, *et al.*, Electroless formation of hybrid lithium anodes for fast interfacial ion transport, *Angew. Chem., Int. Ed.*, 2017, **56**, 13070–13077.
- 30 X. Liang, et al., A facile surface chemistry route to a stabilized lithium metal anode, Nat. Energy, 2017, 2, 17119.
- 31 Z. Tu, et al., Fast ion transport at solid-solid interfaces in hybrid battery anodes, Nat. Energy, 2018, 3, 310–316.
- 32 Y. Li, *et al.*, Unraveling the Reaction Mystery of Li and Na with Dry Air, *J. Am. Chem. Soc.*, 2023, **145**, 10576–10583.
- 33 W. Zhou, *et al.*, High-Energy Sn–Ni and Sn–Air Aqueous Batteries via Stannite-Ion Electrochemistry, *J. Am. Chem. Soc.*, 2023, **145**, 10880–10889, DOI: **10.1021**/jacs.3c03039.
- 34 H. Zhang, *et al.*, A high-capacity Sn metal anode for aqueous acidic batteries, *Joule*, 2023, 7, 971–985.